JOURNAL OF SPACECRAFT AND ROCKETS
Vol. 42, No. 1, January–February 2005

Stationary Coupling of Hypersonic Nonequilibrium Flows and Thermal-Protection-System Structure

Farid Infed,* Ferdinand Olawsky,* and Monika Auweter-Kurtz†
University of Stuttgart, 70550 Stuttgart, Germany

The aim is to present a method of coupling aerodynamic convective heating, radiative exchange, and thermal conduction. The models that describe heat conduction within thermal-protection-system (TPS) materials and radiative exchange at the surface of space vehicles have been developed to supplement catalysis modeling at the surface with the aim of accurate prediction of the thermal loads during reentry. These models have been developed for the three-dimensional parallel-multiblock (P-MB) URANUS (upwind relaxation algorithm for nonequilibrium flows of the University of Stuttgart) code. The influence of radiative exchange and thermal conduction within the TPS material on the catalysis and the gas state at the surface, and thus on the heat load distribution at the surface, is demonstrated for the reentry vehicles COLIBRI and X-38 with real TPS coating.

Nomenclature

$C_{e,\mathrm{TPS}}$	=	thermal protection system (TPS) element specific heat matrix
$\boldsymbol{C}_i$	=	position vector of the center of surface i
$c_{p,\mathrm{TPS}}$	=	specific heat of the TPS material, J/(kg · K)
D	=	TPS heat conductivity matrix
$e_{\mathrm{vib},i}$	=	vibrational energy of species i, J
F	=	total energy flux at the surface, W/m^2
F_{ij}	=	view factor to see surface S_j from the surface S_i
$F_{\mathrm{vib},k}$	=	vibrational energy flux of the molecular species k, W/m^2
$h_{0,i}$	=	enthalpy of species i, J/kg
I_n, I_s, I_t	=	momentum fluxes in normal and tangential directions (kg · m)/s
J	=	Jacobian
$\boldsymbol{j}_i$	=	mass flux vector at the surface of species i
K	=	shear-stress tensor for viscid fluxes
$K_{e,\mathrm{TPS}}$	=	TPS element diffusion conductivity matrix
$\boldsymbol{L}$	=	vector operator $\partial/\partial x$, $\partial/\partial y$, $\partial/\partial z$
Ma	=	Mach number
$\boldsymbol{N}(\xi, \eta, \zeta)$	=	shape function vector
$\boldsymbol{n}$	=	normal vector to the surface
$\boldsymbol{P}_i$	=	position vector of point i
p	=	pressure, Pa
$\boldsymbol{Q}_{e,\mathrm{TPS}}$	=	TPS nodal thermal load vector
$\boldsymbol{q}$	=	heat-conduction flux vector of the gas phase
$q_{i,\mathrm{rad}}$	=	radiative flux received by surface i, W/m^2
$q_{j,\mathrm{rad}}$	=	radiative flux emitted by surface j, W/m^2
$\boldsymbol{q}_{\mathrm{rad}}$	=	radiative heat-flux vector
$\boldsymbol{q}_{\mathrm{TPS}}$	=	heat-conduction flux vector of the TPS material
$\boldsymbol{r}$	=	position vector between the center of S_i and S_j
r, ϕ, φ	=	spherical coordinates
S_a	=	projected surface of S_i in the direction $S_{i,j}$, m^2
S_j	=	surface j, m^2
$\boldsymbol{T}_{e,\mathrm{TPS}}$	=	TPS nodal temperature vector
T_j	=	temperature of surface S_j, K
$T_{\mathrm{vib},k}$	=	vibrational excitation temperature of the molecular species k, K
$\boldsymbol{t}, \boldsymbol{s}$	=	tangential vectors at the surface
$\boldsymbol{V}$	=	velocity vector of the gas at the surface
Vol_e	=	TPS element volume, m^3
v	=	velocity of the space vehicle, m/s
x, y, z	=	Cartesian coordinates
Z_i	=	mass flux of particles of species i, kg/s
γ	=	recombination coefficient
Δt_e	=	TPS element time step, s
ε_j	=	emission coefficient of surface S_j
λ_p	=	TPS longitudinal heat-conduction coefficient, W/m · K
$\lambda_{\mathrm{vib},k}$	=	vibrational heat-conductivity coefficient of the molecular species k in the gas phase, W/m · K
λ_0	=	TPS transversal heat-conduction coefficient, W/m · K
μ	=	viscosity coefficient, kg/m · s
$\boldsymbol{\nu}$	=	viscous dissipation flux vector
ξ, η, ζ	=	TPS element local coordinates
ρ_k	=	density of species k, kg/m^3
ρ_{TPS}	=	TPS material density, kg/m^3
Ω_{ij}	=	solid angle to see surface S_j from surface S_i, rad

Subscripts

k	=	caused by reaction k
rs	=	reflected or scattered

Superscripts

m	=	time index
+	=	leaving the surface
-	=	coming to the surface

Introduction

FOR the development of reusable space transport systems, a detailed prediction of the thermal loads during the reentry is essential. A partially catalytic thermal-protection-system (TPS) design would provide a lower weight system, although reliability would need to be proven. The P-MB URANUS code for hypersonic nonequilibrium flows has been developed at the Institute of Space Systems of the University of Stuttgart for an accurate prediction of the thermal loads.

An example of such a reentry vehicle is the X-38. The vehicle is thermally highly loaded for a large trajectory range. It is equipped with an advanced reusable TPS. This consists of SiC-based ceramics at the high-temperature areas such as stagnation point and body-flap regions, and SiO_2 shuttle tiles for the cooler surface areas. Along the upper trajectory, a dissociated, laminar nonequilibrium flow exists,

Presented as Paper 2003-3984 at the 16th Computational Fluid Dynamics Conference, Orlando, FL, 23–26 June 2003; received 12 July 2003; revision received 26 January 2004; accepted for publication 26 January 2004.

*Ph.D. Student, Institute of Space Systems, Pfaffenwaldring 31.

†Professor, Institute of Space Systems, Pfaffenwaldring 31. Associate Fellow AIAA.

which leads to significant catalytic reactions at the surface. Redox reactions coupled to catalytic reactions and leading to passive and active oxidation can become important in the high-temperature areas. Up to now, the heat-shield design has been mostly based on the fully catalytic design assumption. In the present paper steady-state surface-temperature distributions are computed with the P-MB URANUS nonequilibrium code. The influential gas-surface interaction is taken into account by a global catalysis model using the temperature-dependent overall recombination coefficients for SiC and SiO_2 as measured by Stewart.[1] With this formulation the measured forebody surface heat flux along the integral C/C-SiC heat shield of the MIRKA[2] capsule was satisfactorily reconstructed along the trajectory. Preflight surface-temperature uncertainties with reference to the fully catalytic design assumption have also been computed for the X-38 in the past.[3,4]

As is well known, some of the resulting heat flux at the surface of space vehicles during the reentry is radiated away. In the case that the entire contour is convex, the radiation is not hampered, but for concave configurations, such as for the X-38 with body flap, there are surface elements that see each other. This creates a complicated pattern of absorption and emission of radiated heat on such elements leading to a significant increase in the surface temperature. This phenomenon can be treated by a view factor approach, where a visibility coefficient for every surface element is computed. A practical method to compute the view factors is presented here. This paper also describes how radiative exchange and the resulting radiative heat fluxes are coupled with the flowfield in order to obtain a steady-state solution by P-MB URANUS.

The trajectory path of the reentry vehicle X-38, as an example, shows that it experiences a quasi-steady heat load for nearly 900 s with no significant changes of flight parameters (body-flap deflection or angle of attack of the vehicle).[5,6] Previous experiments in the plasma wind tunnels[7] with TPS material probes (SiO_2, SiC), which back-face is isolated by a KAPYROK™ insulator material (aluminumoxide insulator as it is foreseen for the X-38), showed that the heating of the material probes with the same thickness as is used for X-38 reaches a steady state after 70 s. Thus, the state of the TPS and the flowfield is stationary for a significant amount of time.

The TPS materials just mentioned have a heat-conduction behavior that significantly influences the temperature distribution at the surface and thus the gas state. One approach to take this phenomenon into account is to take the thermal equilibrium heat load distribution at the surface from the flow solver as input for an external heat-conduction solver for the TPS, which then calculates a temperature distribution at the surface. This distribution is then put back into the flow solver to recalculate a new gas state and thus a new surface heat load distribution. The procedure is repeated until convergence is achieved for the coupling of both solvers.[8] This method is very time consuming and not practical for large three-dimensional simulations. This paper also describes the coupling of the heat conduction within the TPS materials with the flowfield by using a finite element model, which calculates the temperature of the TPS due to convective heating from the flow.

To ensure accurate modeling, experimentally obtained temperature-dependent emissivity, conduction coefficients and heat capacity coefficients for real TPS materials (C/SiC and SiO_2) have been used.

P-MB URANUS Code

In the P-MB URANUS nonequilibrium Navier–Stokes code the governing equations are solved in a fully coupled finite volume formulation.[9] The Navier–Stokes equations consist of five species continuity equations for N_2, O_2, NO, N, and O, three momentum equations, the total energy equation, and three vibrational energy equations for the molecular species N_2, O_2, and NO.

The discretization of the inviscid fluxes of the governing equations is performed in the physical space by a Godunov-type upwind scheme employing a gas kinetic flux-vector-splitting[10] solver, whereas the viscous fluxes are discretized in the transformed computational space by central differences on structured multiblock grids using formulas of second-order accuracy.

Thermochemical relaxation processes in the gas phase are accounted for by the multiple temperatures coupled-vibration-chemistry-vibration model.[11,12] The influence of vibrational excitation on chemistry and the influence of chemical reactions on vibration are modeled consistently in the source terms of the conservation equations.

In dissociated reentry flows strong gradients are observed in density, temperatures, and velocities. To describe the exchange of mass, momentum, and energy under these conditions, Chapman–Cowling's first approximations for the transport coefficients, translational thermal conductivity of heavy particles, viscosity and mass diffusion[13] were implemented.

To calculate the steady-state solution of the finite volume Navier–Stokes equations, implicit Euler time differencing with the usual Taylor-series linearization is applied. The resulting linear system has to be solved for each time step. For $\Delta t \to \infty$ the scheme is exactly Newton's method. It is not necessary for Newton's method to compute the Jacobian exactly. Approximations can be made to reduce memory requirement. For this reason, the Jacobian is presently only computed with first-order inviscid fluxes and a thin shear layer approximation for the viscous fluxes. So, the resulting matrix consists of seven blockdiagonals with 12×12 blocks. The linear system is solved with the Jacobi line-relaxation method. To accelerate the code, the Krylov subspace methods generalized minimal residual (GMRES), biconjugate gradients stabilized method (BiCGstab), conjugate gradient squared (CGS), transpose-free quasi-minimum residual method (TFQMR), and quasi-minimal residual conjugate gradient stabilized (QMRCGstab) with a vectorizable incomplete lower–upper (ILU)-preconditioner have been implemented.[14]

The newly designed P-MB URANUS code[15] is able to deal with nearly any kind of structured multiblock meshes, which enables it to deal with complex reentry vehicle geometry.

In a multiblock mesh, beside the surface boundary, flow boundaries (inflow, outflow, symmetry) can occur at each of the six block sides. The P-MB URANUS code is able to handle data exchange for both exact face-to-face and multiple-face mesh blocks neighbors matching, which is the case for the mesh used for the X-38 simulations presented here. The data exchange in P-MB URANUS is performed by message passing interface (MPI). Hence, the portability of the code on widely used supercomputers like NEC SX-5, Cray T3E, or Hitachi SR8000 is guaranteed.

To maintain second order in discretization and extrapolation, the data exchange occurs at the block boundary over an intersection zone (domain overlapping) of two cells.

Different blocks can have different local coordinate directions. This has to be considered when exchanging data between two block neighbors. The necessary data conversion is done during the communication and is hidden from the application.

To obtain the full performance of the system used, the load-balancing tool JOSTLE[16] was implemented into the P-MB URANUS code. The attached load-balancing tool is able to find an optimal distribution of the blocks to the available processors in most cases.

The data structure of the newly developed parallel multiblock extension is already prepared to be able to cope with the next step, adaptive mesh refinement, which is still under development.

Boundary Conditions

A slip model, which is able to predict chemical and thermal nonequilibrium effects at the surface of reentry vehicles, has been implemented into the P-MB URANUS. It is based on a previous model developed by Daiß[17] and has been extended for three-dimensional parallel multiblock applications.[18]

The basic idea of the modeling is balancing incoming and outgoing particles, momentum, and energy fluxes at the surface. The calculation of all fluxes is described in detail in Ref. 18.

The mass source terms have to be balanced by the mass flux normal to the surface. Thus we get

$$\boldsymbol{j}_i \cdot \boldsymbol{n}^T = Z_i^+ - Z_i^- \tag{1}$$

The mass flux of particles leaving the surface consists of the flux of particles that have been reflected or scattered at the surface and the fluxes that are the result of chemical reactions at the surface:

$$Z_i^+ = Z_{rs,i}^+ + \sum_{k=1}^{3} Z_{k,i}^+ \tag{2}$$

The reactions accounted for at the surface are

$$\mathrm{N} + \mathrm{N} \rightarrow \mathrm{N}_2$$

$$\mathrm{O} + \mathrm{O} \rightarrow \mathrm{O}_2$$

$$\mathrm{NO} + \mathrm{NO} \rightarrow \mathrm{N}_2 + \mathrm{O}_2$$

To calculate the reflected fluxes, we use temperature-dependent overall recombination coefficients for finite-rate catalytic TPS materials (SiC, SiO_2), which were measured by Stewart.[1] These are used to determine the fluxes that underwent a chemical reaction at the surface, and then, since fluxes coming to the surface are known, the reflected fluxes are computed, that is,

$$Z_{k,i}^+ = \gamma_k Z_i^- \tag{3}$$

with $\gamma = f(T)$. The recombination coefficients γ have been calibrated along a surface-temperature range between 300 and 2000 K as shown in Figs. 1 and 2.

From the continuum theory we know that the momentum fluxes to a surface are the projection of the momentum tensor on the normal vector of the surface. Considering that the velocity has tangential terms on the surface, the resulting boundary conditions for the momentum equations of the Navier–Stokes equations are

$$p - \boldsymbol{n} \cdot \mu K \cdot \boldsymbol{n}^T = I_n^+ - I_n^- \tag{4}$$

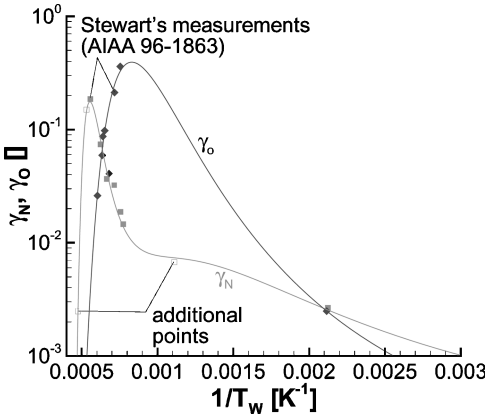

Fig. 1 Recombination coefficients for SiC.

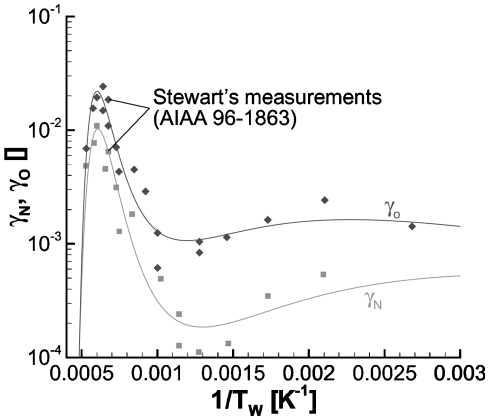

Fig. 2 Recombination coefficients for SiO_2.

$$-\boldsymbol{s} \cdot \mu K \cdot \boldsymbol{n}^T = I_s^+ - I_s^- \tag{5}$$

$$-\boldsymbol{t} \cdot \mu K \cdot \boldsymbol{n}^T = I_t^+ - I_t^- \tag{6}$$

For the vibrational energy boundary equations we get

$$[\boldsymbol{j}_k \cdot e_{\mathrm{vib}}^-(T_{\mathrm{vib},k}) - \lambda_{\mathrm{vib},k} \nabla T_{\mathrm{vib},k}] \cdot \boldsymbol{n} = F_{\mathrm{vib},k}^+ - F_{\mathrm{vib},k}^- \tag{7}$$

Finally the boundary condition for the total energy becomes

$$\left[\sum_{i=1}^{5} \boldsymbol{j}_i h_{0,i} + \boldsymbol{q} + \boldsymbol{v}\right] \cdot \boldsymbol{n} = F^+ - F^- \tag{8}$$

with the heat-conduction flux vector

$$\boldsymbol{q} = -\left[\lambda_{\mathrm{trans}} \nabla T + \sum_{k=1}^{3} (\lambda_{\mathrm{vib},k} \nabla T_{\mathrm{vib},k} + \lambda_{\mathrm{rot},k} \nabla T_{\mathrm{rot},k})\right] \tag{9}$$

and the contribution of the viscous dissipation to the heat flux

$$\boldsymbol{v} = -\mu K \cdot \boldsymbol{V} \tag{10}$$

The rotational and translational heat-conduction coefficients are also taken from the gas phase.

Radiative Exchange at the Surface

Every surface, which has a temperature above absolute zero, emits radiative flux in all directions. Thus, if a surface element is able to see another one, each surface receives a part of the flux emitted by the other one.

In this section, we will show how the radiative flux received by an elementary surface i from another surface j is calculated. Every body emits an energy that depends on its temperature. The radiation emitted by S_1 in the direction of S_2 leads to an increases of surface temperature T_2. The same phenomenon applies to S_2 such that the temperature T_1 of S_1 increases as well. As consequence, a modification of T_1 changes the flux emitted from S_1. To evaluate the radiative flux received by a surface S_i from all other surfaces j, we write

$$q_{i,\mathrm{rad}} = \sum_j F_{ij} q_{j,\mathrm{rad}} \tag{11}$$

According to Stefan–Boltzmann's law of radiation, we get

$$q_{j,\mathrm{rad}} = \varepsilon_j \cdot \sigma \cdot T_j^4 \tag{12}$$

The emission coefficients for the widely used TPS materials (C/SiC and SiO_2) are temperature dependent and are considered so in our modeling. Further details considering this issue will follow later in this paper. First, we will explain the calculation of view factors for two surfaces, and then we consider the case how each surface element sees all other surface elements. To simplify the computation, we will consider that our surfaces are Lambertian, that is, the luminance L is independent of the emission direction:

$$L(\theta) = L \tag{13}$$

where θ is the emission direction. The notations are shown in Fig. 3.

The hemispherical flux emitted from S_1 in all directions is

$$q_{1,\mathrm{rad}} = \pi L_1 S_1 \tag{14}$$

and the flux emitted from S_1 in the direction of S_2 is

$$q_{1\rightarrow 2,\mathrm{rad}} = L_1 S_a \cdot \Omega_{12} \tag{15}$$

with $S_a = S_1 \cdot \cos\theta_1$. At last we have

$$F_{12} = q_{1\rightarrow 2,\mathrm{rad}} / q_{1,\mathrm{rad}} = (\Omega_{12} |\cos\theta_1|)/\pi \tag{16}$$

We evaluate the cosines of the angles θ_1 using the scalar product

$$\cos(\theta_1) = (\boldsymbol{n}_1 \cdot \boldsymbol{r})/(|\boldsymbol{n}_1| \cdot |\boldsymbol{r}|) \tag{17}$$

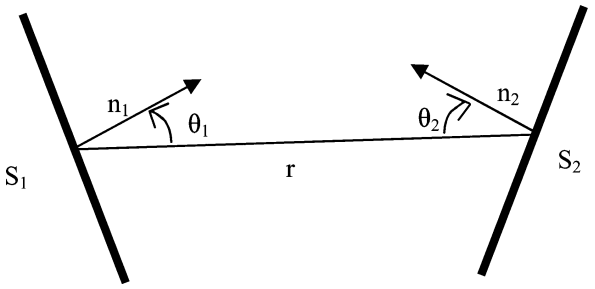

Fig. 3 Geometrical notation for the calculation of the view factors.

A TPS tile emits radiation only from the side where the normal vector points into space. The other side is coated with insulation that absorbs the radiation, so that the view factor is considered to be null when $\boldsymbol{n}_1 \cdot \boldsymbol{n}_2 \geq 0$. A surface can-not see itself; thus, $F_{ii} = 0$. The computation of every view factor is done without simplification. If we have n surfaces, we calculate $n(n-1)$ view factors. If a surface S_i can see a surface S_j but if S_j is totally under the horizon of S_i, S_i would see the isolated side of S_j. In this case, the view factor F_{ij} has to be null even if the computation of F_{ij} returns a nonnull value. The property $S_i \cdot F_{ij} = S_j \cdot F_{ji}$ is not used, even if it could reduce the computation time. With the approach using the horizon, the surfaces S_i can be modified so that only its visible part is considered. The minimum between $S_i \cdot F_{ij}$ and $S_j \cdot F_{ji}$ is taken because if there is a computational error for one of the two view factors F_{ij} or F_{ji}, two identical surfaces could emit different fluxes, which is not possible.

Two conditions have to be fullfilled by the model. The first is that every view factor must have a numerical value between 0 and 1:

$$0 \leq F_{ij} \leq 1 \tag{18}$$

$F_{ij} = 0$ if surface element i emits no energy in the direction of surface element j, and $F_{ij} = 1$ if surface element j receives all of the energy emitted by S_i. Hence the second property is that

$$\sum_j F_{ij} \leq 1 \tag{19}$$

because there is no creation of energy. Now we explain how we calculate the solid angle that is necessary for the computation of the view factors. To show the method, we will determine the solid angle of surface S_2 as seen from surface S_1, where S_2 is composed of four points $\boldsymbol{P}_1, \boldsymbol{P}_2, \boldsymbol{P}_3$, and $\boldsymbol{P}_4$. We begin by converting the Cartesian coordinates of the four points in spherical coordinates to simplify the calculation of the projection of the surface S_2. Then, we keep only the part of S_2 visible by S_1. Finally, we return to Cartesian coordinates to determine the area of the projected surfaces. We consider the sphere centered at $\boldsymbol{C}_1$, passing by point $\boldsymbol{C}_2$ with radius r. To determine the spherical coordinates, we use a local basis $(\boldsymbol{t}_1, \boldsymbol{s}_1, \boldsymbol{n}_1)$. We denote $x = \boldsymbol{t}_1 \cdot (\boldsymbol{P}_i - \boldsymbol{C}_1)$ and $y = \boldsymbol{s}_1 \cdot (\boldsymbol{P}_i - \boldsymbol{C}_1)$ and obtain the coordinates of the point $\boldsymbol{P}_i$ with the following relations:

$$r = |\boldsymbol{C}_2 - \boldsymbol{C}_1| \tag{20}$$

$$r_{p_i} = |\boldsymbol{P}_i - \boldsymbol{C}_1| \tag{21}$$

$$\phi_{P_i} = \cos^{-1}\left[\frac{\boldsymbol{n}_1 \cdot (\boldsymbol{P}_i - \boldsymbol{C}_1)}{|\boldsymbol{P}_i - \boldsymbol{C}_1|}\right] \tag{22}$$

$$\varphi_{P_i} = \tan^{-1}\left(\frac{y}{x}\right), \qquad x > 0 \tag{23a}$$

$$\varphi_{P_i} = \tan^{-1}\left(\frac{y}{x}\right) + \pi, \qquad x < 0, \qquad y > 0 \tag{23b}$$

$$\varphi_{P_i} = \tan^{-1}\left(\frac{y}{x}\right) - \pi, \qquad x < 0, \qquad y < 0 \tag{23c}$$

$$\varphi_{P_i} = \frac{\pi}{2}, \qquad x = 0, \qquad y > 0 \tag{23d}$$

$$\varphi_{P_i} = -\frac{\pi}{2}, \qquad x = 0, \qquad y < 0 \tag{23e}$$

We notice that $-\pi \leq \varphi \leq +\pi$ and $0 \leq \phi \leq \pi$. When we calculate the solid angle, it is important to know which part of S_2 is effectively seen by the surface S_1. That is what we call the horizon problem. In fact we must calculate S_2^*, which is part of the surface S_2 over the horizon defined by the plane $(\boldsymbol{t}, \boldsymbol{s})$. To accomplish this calculation, we begin by ordering the points so that

$$\phi_{P_1} \geq \phi_{P_2} \geq \phi_{P_3} \geq \phi_{P_4} \tag{24}$$

ϕ_{P_i} indicates the position of $\boldsymbol{P}_i$ with regard to the horizon. To calculate the area of the surface over the horizon, we have five possible configurations that correspond to the position of the horizon:

$$\phi_{P_1} \leq \pi/2 \tag{25a}$$

$$\phi_{P_1} > \pi/2, \qquad \phi_{P_2} < \pi/2 \tag{25b}$$

$$\phi_{P_2} \geq \pi/2, \qquad \phi_{P_3} < \pi/2 \tag{25c}$$

$$\phi_{P_3} \geq \pi/2, \qquad \phi_{P_4} < \pi/2 \tag{25d}$$

$$\phi_{P_4} \geq \pi/2 \tag{25e}$$

Now we have new projected points $\boldsymbol{P}_1^+, \boldsymbol{P}_2^+, \boldsymbol{P}_3^+, \boldsymbol{P}_4^+$ with the following relations:

$$x_{P_i^+} = |\boldsymbol{C}_2 - \boldsymbol{C}_1| \cdot \sin\left(\phi_{P_i}\right) \cdot \cos\left(\varphi_{P_i}\right) \tag{26a}$$

$$y_{P_i^+} = |\boldsymbol{C}_2 - \boldsymbol{C}_1| \cdot \sin\left(\phi_{P_i}\right) \cdot \sin\left(\varphi_{P_i}\right) \tag{26b}$$

$$z_{P_i^+} = |\boldsymbol{C}_2 - \boldsymbol{C}_1| \cdot \cos\left(\phi_{P_i}\right) \tag{26c}$$

The coupling of the radiative exchange at the surface is given by extending Eq. (8) for each surface cell i by adding the radiative term given by Eq. (11):

$$\left[\sum_{i=1}^{5} \boldsymbol{j}_i h_{0,i} + \boldsymbol{q} + \boldsymbol{v} + \boldsymbol{q}_{\text{rad}}\right] \cdot \boldsymbol{n} = F^+ - F^- \tag{27}$$

Herein the left-hand side of Eq. (27) denotes the new total heat flux at the surface.

Heat Conduction in the TPS

In this section we will present a finite element based model, which gives a new temperature distribution at the surface taking into account thermal conduction within the TPS. Just for convenience, we would like to emphasize that this model works such that the heat-conduction equations are solved for each time step of the flow solver. The resulting surface temperatures, and thus the TPS conduction heat fluxes, are then inserted into Eq. (27).

For a differential control solid TPS volume, the first law of thermodynamics, which states that thermal energy is conserved,[19] can be written as follows:

$$\rho_{\text{TPS}} c_{p,\text{TPS}} \left(\frac{\partial T_{\text{TPS}}}{\partial t} + \boldsymbol{v}_{\text{TPS}}^T \boldsymbol{L} T_{\text{TPS}}\right) + \boldsymbol{L}^T \boldsymbol{q}_{\text{TPS}} = \boldsymbol{S}_{\text{TPS}} \tag{28}$$

where $\boldsymbol{v}_{\text{TPS}}$ is the velocity vector for mass transport of heat in the TPS and $\boldsymbol{S}_{\text{TPS}}$ is the source term vector for heat generation rate per volume unit. Fourier's law is applied to give the heat-flux vector in relation to the thermal gradients:

$$\boldsymbol{q}_{\text{TPS}} = -D \cdot \boldsymbol{L} T_{\text{TPS}} \tag{29}$$

where

$$D = \begin{bmatrix} \lambda_p & 0 & 0 \\ 0 & \lambda_0 & 0 \\ 0 & 0 & \lambda_p \end{bmatrix} \tag{30}$$

As we mentioned before, we use a finite element approach to solve Eq. (28) for the nodal temperature. To do so, we have to modify the

equation by introducing the concept of shape functions to provide a relationship between the TPS volume data and the data at the nodes that define our TPS control volume element. The advantage of this approach is that any kind of grid and element constellation of the grid can be treated. P-MB URANUS automatically generates a TPS grid. Staring from the flow mesh, the surface geometry of reentry vehicle is given. Using a few input parameters such as element type, cell number, and TPS material widths, the mesh is calculated in the preprocessing phase. Both flow mesh and TPS grid share the same nodes at the surface. As stated in Eq. (28), the temperature T_{TPS} varies both in time and space. This dependency for each element is separated as

$$T_{\mathrm{TPS}} = \boldsymbol{N}^T \cdot \boldsymbol{T}_{e,\mathrm{TPS}} \tag{31}$$

The origin of the local coordinates ξ, η, and ζ of an element's shape functions is at the element's geometrical center and

$$-1 \leq \xi, \eta, \zeta \leq 1 \tag{32}$$

Thus the time derivatives of Eq. (31) can be written as

$$\frac{\partial T_{\mathrm{TPS}}}{\partial t} = \boldsymbol{N}^T \cdot \frac{\partial \boldsymbol{T}_{e,\mathrm{TPS}}}{\partial t} \tag{33}$$

Furthermore, let

$$\boldsymbol{L}T_{\mathrm{TPS}} = B \cdot \boldsymbol{T}_{e,\mathrm{TPS}} \tag{34}$$

with

$$B = \boldsymbol{L} \cdot \boldsymbol{N}^T$$

The calculation of B is given in Ref. 18. After considering the boundary conditions at a surface Γ, neglecting the effects of mass transport within the solid TPS material and assuming that no heat generation occurs within the TPS, Eq. (29) becomes

$$\rho_{\mathrm{TPS}} \int_{\mathrm{vol}} c_{p,\mathrm{TPS}} \boldsymbol{N} \cdot \boldsymbol{N}^T \,\mathrm{d(Vol)} \frac{\partial \boldsymbol{T}_{e,\mathrm{TPS}}}{\partial t} + \int_{\mathrm{vol}} B^T D B \,\mathrm{d(Vol)} \boldsymbol{T}_{e,\mathrm{TPS}}$$

$$+ \int_{\Gamma} \boldsymbol{N} \cdot \boldsymbol{n}_{\Gamma}^T D B \,\mathrm{d}(\Gamma) \boldsymbol{T}_{e,\mathrm{TPS}} = \boldsymbol{Q}_{e,\mathrm{TPS}} \tag{35}$$

where $\boldsymbol{n}_{\Gamma}$ is the unit outward normal vector of the TPS grid boundary surface Γ. Equation (35) can be rewritten as

$$C_{e,\mathrm{TPS}} \frac{\partial \boldsymbol{T}_{e,\mathrm{TPS}}}{\partial t} + K_{e,\mathrm{TPS}} \boldsymbol{T}_{e,\mathrm{TPS}} = \boldsymbol{Q}_{e,\mathrm{TPS}} \tag{36}$$

Because we are only interested in the stationary solution of Eq. (36), we approximate the time derivative of the nodal temperature by

$$\frac{\partial \boldsymbol{T}_{e,\mathrm{TPS}}}{\partial t} = \frac{\boldsymbol{T}^m_{e,\mathrm{TPS}} - \boldsymbol{T}^{m-1}_{e,\mathrm{TPS}}}{\Delta t} \tag{37}$$

Equation (36) is then

$$(C_{e,\mathrm{TPS}}/\Delta t)(\boldsymbol{T}_{e,\mathrm{TPS}})^m + K_{e,\mathrm{TPS}}(\boldsymbol{T}_{e,\mathrm{TPS}})^m$$

$$= (\boldsymbol{Q}_{e,\mathrm{TPS}})^m + (C_{e,\mathrm{TPS}}/\Delta t)(\boldsymbol{T}_{e,\mathrm{TPS}})^{m-1}$$

or

$$\bar{K}_{e,\mathrm{TPS}}(\boldsymbol{T}_{e,\mathrm{TPS}})^m = (\boldsymbol{Q}_{e,\mathrm{TPS}})^m + (C_{e,\mathrm{TPS}}/\Delta t)(\boldsymbol{T}_{e,\mathrm{TPS}})^{m-1} \tag{38}$$

Equation (38) reflects the physics for each element. Thus, an assembly process for the entire TPS grid of each block has to be performed before solving Eq. (38) for the nodal temperature. For stability criteria,[20]

$$\Delta t_e \leq \frac{\rho_{e,\mathrm{TPS}} \cdot c_{e,\mathrm{TPS}} \cdot \mathrm{Vol}_e}{2 \max(\lambda_0, \lambda_p)} \tag{39}$$

The biggest time step possible in a TPS grid block is used for solving Eq. (38).

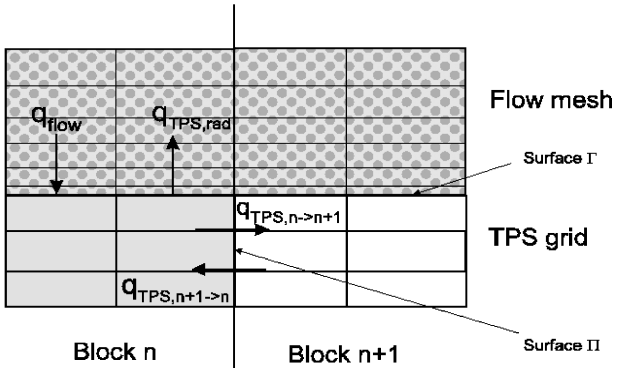

Fig. 4 Flux composition at the surface and heat-conduction flux exchange between two neighboring TPS grid blocks.

The nodal load vector of Eq. (38) contains the heat flux from the flow side and the radiated heat flux from the surface of the TPS material, which is the only heat sink for this model, and the TPS heat flux of the neighboring blocks. In fact, the nodal load vector is the key for the parallelization of the heat-conduction model. The common method of parallelizing Eq. (38) is by assembling the equation over all blocks and then solving the resulting linear system by methods of domain decomposition on certain number of processsors.[21]

This method would cause an imbalance of the calculation loads of each processor, because the TPS solver in the P-MB URANUS code has to be treated on each processor, which has a block with surface boundary. Figure 4 gives an overview of the composition of the nodal load vector. As seen in Fig. 4, for the nodes that are at the surface, the heat load vector contains the heat flux from the flow taken from Eq. (27) and the radiated flux. Thus,

$$(\boldsymbol{Q}_{e,\mathrm{TPS}})^m = \int_{\Gamma} -\left[\sum_{i=1}^{5} \boldsymbol{j}_i h_{0,i} + \boldsymbol{q} + \boldsymbol{v} + \boldsymbol{q}_{\mathrm{rad}} \right] \cdot \boldsymbol{n}$$

$$- \varepsilon \cdot \sigma \cdot \left(\boldsymbol{T}^{m-1}_{e,\mathrm{TPS}} \right)^4 \mathrm{d}\Gamma \tag{40}$$

For the nodes at the block boundaries, we take the TPS heat flux from the neighboring block as input for the current block,

$$(\boldsymbol{Q}_{e,\mathrm{TPS}})^m = \int_{\Pi} \boldsymbol{N} \cdot \boldsymbol{n}_{\Pi}^T D \boldsymbol{L} \boldsymbol{N}^T (\boldsymbol{T}_{e,\mathrm{TPS}})^{m-1} \,\mathrm{d}\Pi \tag{41}$$

Because the backface of the TPS is insulated, the heat flux at this side is considered to be null.

After the assembly process, we solve the heat-conduction equations (38), which have the form $Ax = b$ by the conjugate gradient method[‡] after preconditioning with the inverse of the main diagonal of A.

For the final step, the coupling is given by supplementing Eq. (27) with the TPS heat conduction flux vector so that we obtain

$$\left[\sum_{i=1}^{5} \boldsymbol{j}_i h_{0,i} + \boldsymbol{q} + \boldsymbol{q}_{\mathrm{rad}} + \boldsymbol{v} + \boldsymbol{q}_{\mathrm{TPS}} \right] \cdot \boldsymbol{n} = F^+ - F^- \tag{42}$$

with

$$\boldsymbol{q}_{\mathrm{TPS}} = D \boldsymbol{L} \boldsymbol{N}^T \cdot \boldsymbol{T}_{e,\mathrm{TPS}} \tag{43}$$

Experimental Data for the Modeling

We use experimental data for our modeling. All data are temperature dependent and fitted by polynomial functions over a temperature range that covers the typical range of use (300–2200 K). The densities of the materials are considered to be temperature independent. We use 3200 kg/m^3 for C/SiC and 2197 kg/m^3 for SiO_2.[22] Figures 5–8 show the measured values (symbols) and the corresponding fitting functions.

[‡]Data available online by anonymous FTP to WARP.CS.CMU.EDU (128.2.209.103) as quake-papers/painless-conjugate-gradients.ps [cited 15 Oct. 2002].

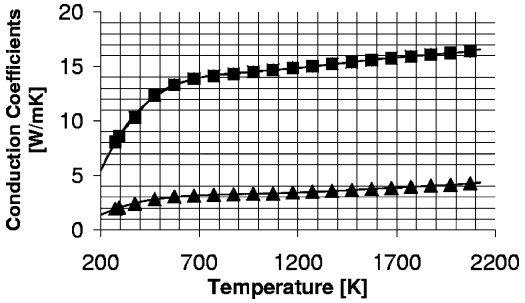

Fig. 5 Heat-conduction coefficients for C/SiC (■, longitudinal; ▲, transversal).

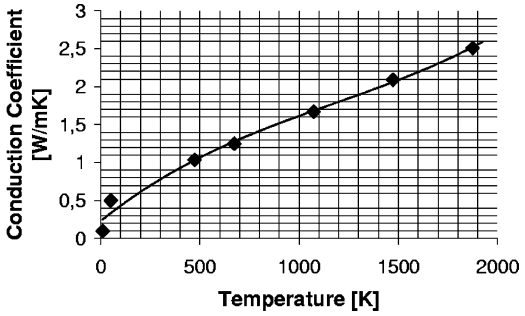

Fig. 6 Heat-conduction coefficients for SiO_2.

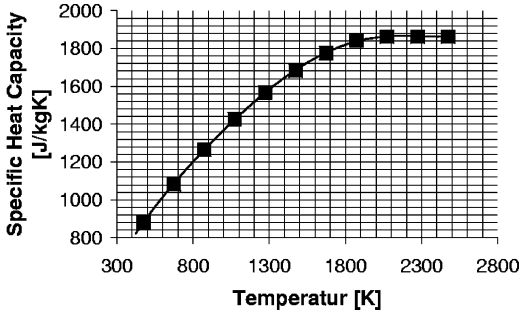

Fig. 7 Specific heat capacity for C/SiC.

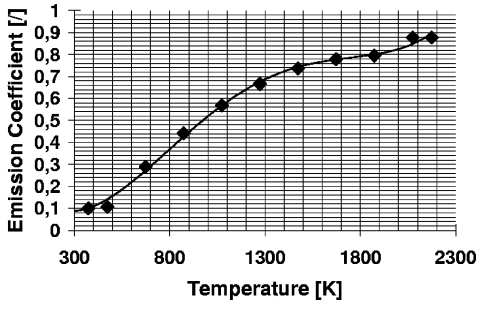

Fig. 8 Emission coefficients for C/SiC.

The corresponding fitting polynomials are

λ-C/SiC:

$$\lambda_p = 4.64016992789728 \times 10^{-15} \cdot T_w^5 - 3.29345481116632 \times 10^{-11} \cdot T_w^4 + 9.06467896911026 \times 10^{-8} \cdot T_w^3 - 1.20562544627109 \times 10^{-4} \cdot T_w^2 + 7.90264328097808 \times 10^{-2} \cdot T_w - 6.24818856805873$$

$$\lambda_0 = 1.02091145725730 \times 10^{-15} \cdot T_w^5 - 7.28768552512860 \times 10^{-12} \cdot T_w^4 + 2.01276446499472 \times 10^{-8} \cdot T_w^3 - 2.64846669104229 \times 10^{-5} \cdot T_w^2 + 1.70840675354520 \times 10^{-2} \cdot T_w - 1.14260670379805$$

λ-SiO_2:

$$\lambda_p = \lambda_0 = 2.84980259590809 \times 10^{-10} \cdot T_w^3 - 1.00477567335607 \times 10^{-6} \cdot T_w^2 + 2.10470691383035 \times 10^{-3} \cdot T_w + 2.30200395365815 \times 10^{-1}$$

ε-SiO_2, $\varepsilon = 0.89$ (see Ref. 23), c_p-C/SiC, ($T_w < 2073.15$ K):

$$c_p = +2.568809878123 \times 10^{-11} \cdot T_w^4 - 1.35574349915567 \times 10^{-7} \cdot T_w^3 - 6.42021696584042 \times 10^{-4} \cdot T_w^2 + 1.22930795134935 \times 10^{-2} \cdot T_w + 3.21678570693030 \times 10^{2}$$

($T_w > 2073.15$ K), $c_p = 1863.0$ J/kgK, c_p-SiO_2 has been taken from the website.[§]

ε-C/SiC:

$$\varepsilon = -8.38642669240192 \times 10^{-15} \cdot T_w^4 + 1.11867854310319 \times 10^{-10} \cdot T_w^3 - 5.62657219365013 \times 10^{-7} \cdot T_w^2 + 1.23930426522556 \times 10^{-3} \cdot T_w - 1.20676050349761 \times 10^{-1}$$

Results of COLIBRI and X-38 Simulations

COLIBRI (concept of a lifting body for reentry investigations) has been conceived as a testbed to perform autonomous scientific and technological experiments during a reentry flight. The vehicle is characterized by a blunt-body shape with a nose radius of 0.18 m, as in Fig. 9. In the case of this vehicle, we will only demonstrate the influence of the TPS grid resolution on the temperature distribution at the surface. A more challenging geometry is given by the X-38 (Fig. 10), prototype vehicle for the crew return vehicle, which shall allow quick return of astronauts on the International Space Station to Earth in cases of emergency. The results of X-38 are more interesting for the modeling of heat conduction within the TPS and radiative exchange at the surface, because the geometry of the vehicle has concave shapes and angular parts. In addition there is a change in TPS materials.

The reentry of the COLIBRI and X-38 vehicles is simulated for a trajectory point at 64.6 km with $Ma = 19.8$. The detailed upstream condition data are as follows:

$$p = 12.1707 \text{ N/m}^2$$

$$\rho_{N2} = 1.3813 \times 10^{-4} \text{ kg/m}^3$$

[§]Data available online at http://webbook.nist.gov [cited 20 Sept. 2002].

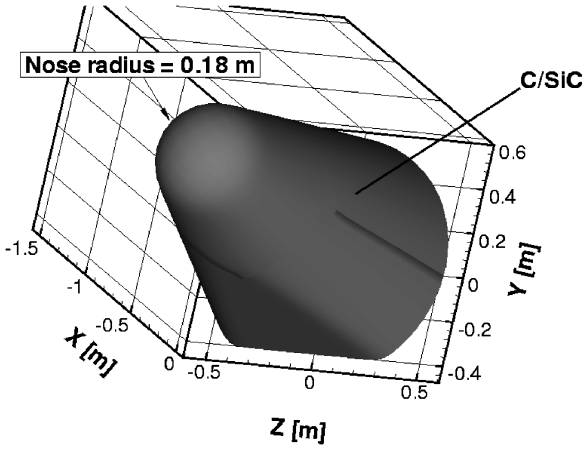

Fig. 9 Geometry and TPS coating of COLIBRI.

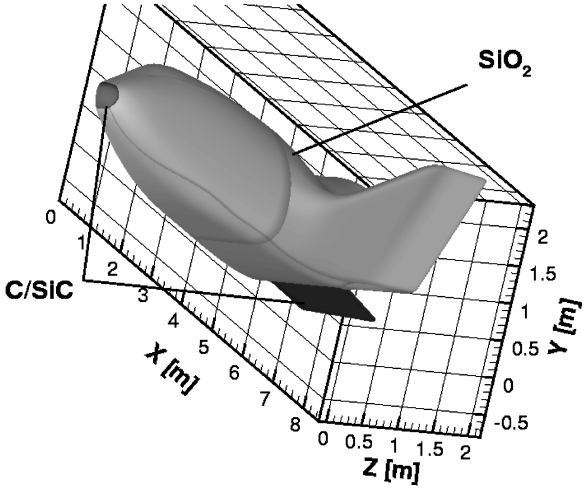

Fig. 10 Geometry and TPS coating of X-38.

$$\rho_{O2} = 4.2371 \times 10^{-5}\ \text{kg/m}^3$$

$$\rho_{NO} = 1.8770 \times 10^{-16}\ \text{kg/m}^3$$

$$\rho_{N} = 8.7621 \times 10^{-17}\ \text{kg/m}^3$$

$$\rho_{O} = 1.0008 \times 10^{-16}\ \text{kg/m}^3$$

$$T_{\text{vib,N2}} = 234.0321\ \text{K}$$

$$T_{\text{vib,O2}} = 234.0321\ \text{K}$$

$$T_{\text{vib,NO}} = 234.0321\ \text{K}$$

$$v = 6085\ \text{m/s}$$

For the considered trajectory point, both vehicles have an angle of attack $\alpha = 40$ deg. The body-flap deflection of the X-38 is $\delta = 20$ deg. The surface-temperature distribution is computed for the real TPS, which is based on SiC and SiO_2 technology. The X-38 nose cap, nose skirt, and chin panel are made by C/SiC and are considered so for the simulations. The rest of X-38's surface is equipped with SiO_2 tiles, which is also taken into account for the simulations discussed here (see Fig. 10). COLIBRI's TPS is completely coated by C/SiC, as in Fig. 9. For the simulations of the X-38, a Deutsches Luft- und Raumfahrtzentrum (DLR) multiblock mesh, which contains wake flow regions, is used. This mesh has 1.02 million cells and consists of 18 initial blocks. Simulations for COLIBRI were performed on a multiblock mesh generated with GridPro[23] consisting of 10 initial blocks with 800,000 cells. For both vehicles, COLIBRI and X-38, the near surface resolution is within the scope of mean free path

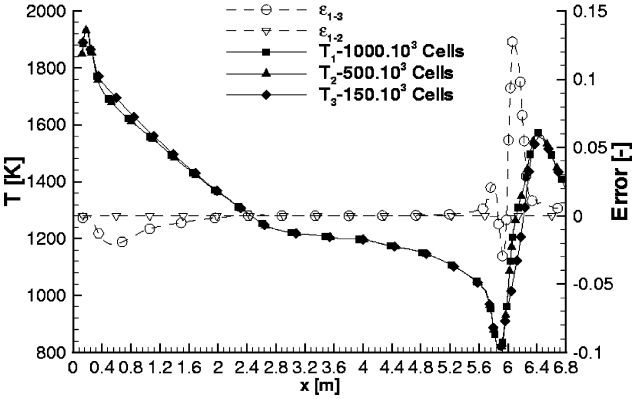

Fig. 11 Temperature distribution along the symmetry line of X-38 with real TPS coating without radiative exchange/TPS heat conduction at 64.6 km with 1 million (T_1), 500,000 (T_2), 150,000 (T_3) cells mesh and the resolution uncertainties $\varepsilon_{1\text{-}3}$ (error between solution T_1 and T_3) and $\varepsilon_{1\text{-}2}$ (error between solution T_1 and T_2).

length (10^{-6} m) and thus sufficient for the prediction of the surface heat flux. The resolution in the normal direction is 80 cells. For the tangential directions, the mesh is resolved by 66 cells for each initial block. This applies for both COLIBRI and X-38. Studies concerning the resolution of the flow meshes for both vehicles have been performed in the past.[9,15] As an example for flow mesh studies, the temperature distribution along the symmetry line of the X-38 with real TPS coating at a trajectory point at 64.6 km is showed for three resolution levels in Fig. 11.

Figure 11 shows, considering the error curves [$\varepsilon_{1\text{-}3} = (T_1\text{-}T_3)/T_1$ and $\varepsilon_{1\text{-}2} = (T_1\text{-}T_2)/T_1$], that the surface temperature or the surface heat flux, the primery concern of the new modeling presented in this paper, is mesh independent after a resolution higher then 500,000 cells. However, for a more reliable solution a 1 million cells resolution is still preferable.

The SiC-based tiles of the X-38's TPS have a thickness of 4×10^{-3} m. For simplification we approximate the SiO_2-based tiles as having the same thickness. The TPS grid consists of finite linear brick elements and is resolved by 20 cells in the orthogonal direction. The resolution in tangential directions is as for the flow mesh.

The simulation for X-38 was performed on an NEC SX-5 computer using six CPUs and requiring 17.8 GB of memory. COLIBRI simulations required between 13.5 and 14.5 GB of memory depending on the resolution of the TPS grid used for the sensitivity study. The TPS material of COLIBRI has the same thickness of the X-38's TPS. The TPS grid resolution is 20, 40, and 60 cells in the orthogonal direction.

The simulation for X-38 ran with a total performance of 9.4 GFLOPS on six NEC-SX5 processors. Courant–Friedrichs–Lewy (CFL) numbers up to 100 have been reached for the computations with a second order flux discretization; higher CFL numbers were possible for first order discretization. On average, each iteration took about 45 s. In total, the simulation took about 25 h of computation.

Figure 12 shows the convergence history of the X-38 with real TPS coating. Both radiative heat exchange and TPS heat-conduction modeling are activated. A significant difference in the convergence history without the modeling presented here[15] has not been observed. The calculation of the residual for the flow solver can be obtained from Ref. 14. The residuals calculation of the TPS heat conduction model is explained in Ref. 16.

The performance for COLIBRI simulations was about 8.1 GFLOPS on five NEC-SX5 processors. CFL numbers up to 500 were possible for second order flux discretization. An iteration took about 39 s. Each simulation case was completed within 17 h. The convergence history for COLIBRI is similar to the one of X-38.

Influence of the TPS Grid Resolution

In this section the influence of the TPS grid resolution on the temperature distribution at the surface is demonstrated in the case of the blunt-body vehicle COLIBRI.

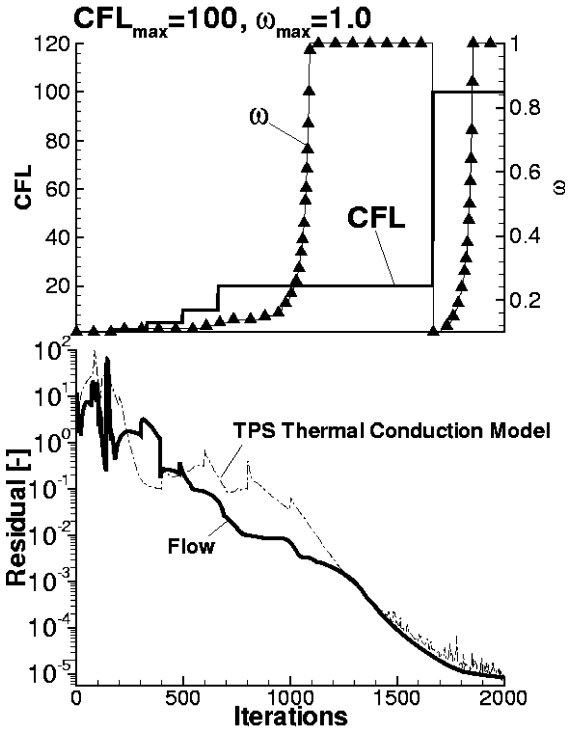

Fig. 12 Convergence history of the X-38 with real TPS coating with radiative heat exchange and TPS heat-conduction modeling.

Figure 13 shows the temperature distribution of COLIBRI with and without heat conduction within the C/SiC TPS material. As expected, the highest temperature is observed at the nose region where the material has to sustain a temperature of 1950 K. The temperature distribution for parts a and b of Fig. 13 is smooth, as is expected for Navier–Stokes simulations. As expected, the heat conduction within the TPS caused a moving of the temperature from the hot windward side to the cooler leeward side of the vehicle. The difference ($\Delta T = T_{S,\mathrm{TPS}} - T_S$) in temperature is not significant for such a blunt-body configuration with a continuous TPS coating, as shown in Fig. 14. The differences were within the range of -20 to $+40$ K. However, the aim of the simulations with COLIBRI was to demonstrate the sensitivity of the solution with regard to the TPS grid resolution. Figure 15 shows the temperature over the contour length in the nose region for three different TPS grid resolutions. It shows that the solution is not sensitive to the resolution of the TPS grid. This result demonstrates that the resolution of 20 cells in orthogonal direction is already adequate and thus further refinement of the 4×10^{-3} m thick TPS grid is unnecessary.

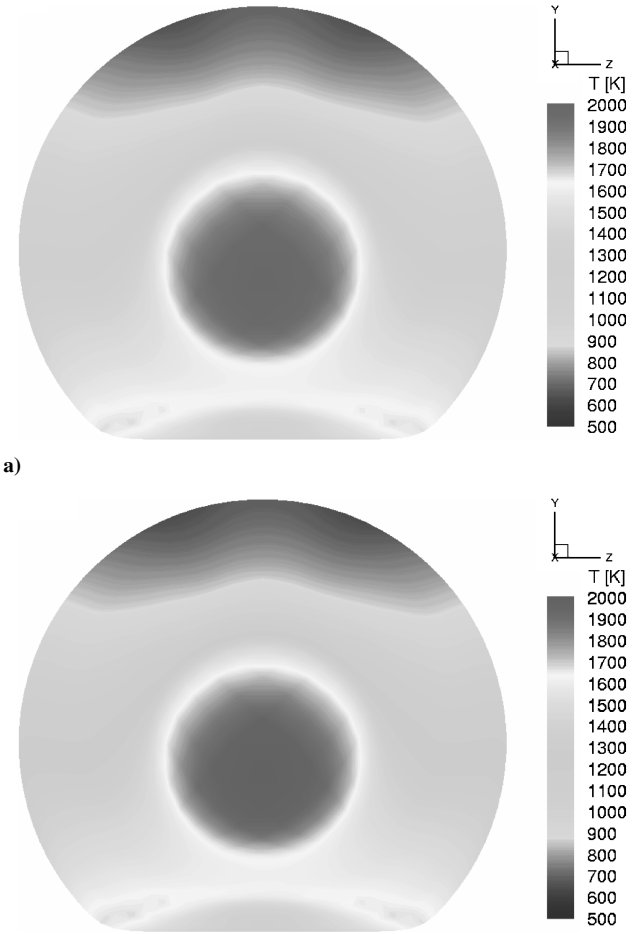

Fig. 13 Temperature distribution at the surface of COLIBRI a) without heat conduction within TPS material and b) with heat conduction within TPS.

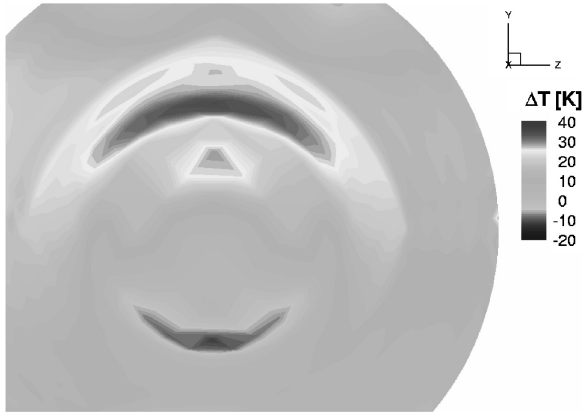

Fig. 14 Distribution of temperature difference at the surface of COLIBRI between solutions with and without heat conduction within TPS material.

Radiative Exchange at the Surface of the X-38

In this section we analyze the impact of the radiative exchange on the surface-temperature distribution in the cavity region of the body flap of the X-38 where radiation effects, as a result of the concave geometry, are, as expected, a driving mechanism and cause important changes in the heat load distribution. Considering the baseline temperature distribution, radiative exchange effects on other parts of the vehicle are negligible. To isolate the effects of radiation, the thermal heat conduction within the TPS materials has not been taken into account for the analysis. Figure 16 shows an increase of the surface temperature at the main body of the X-38, which is coated with SiO_2 tiles, and at the body flap, which is coated with C/SiC. Data extrapolation along "extrapolation line" 1 and 2 (Figs. 17 and 18) gives a closer look at the two hotspots. Figure 17 shows the temperature, recombination coefficients for oxygen and nitrogen, and the temperature difference ΔT between the solution with radiative exchange (symbols) and without radiative exchange at the surface along extrapolation line 1.

The maximum temperature difference is about 400 K. The figure also shows that the recombination of the atomic species has been decreased after taking the radiative exchange into account while a temperature increase can be observed. Concordantly, the surface catalysis is noninvolved at the temperature increase of the SiO_2 tiles.

For the body flap the surface catalysis has a crucial role. From Fig. 18 one can observe that radiative exchange significantly increased the recombination of atomic oxygen, which dominates the temperature distribution along extrapolation line 2. The highest difference in temperature occurs where the difference in recombination has the highest value.

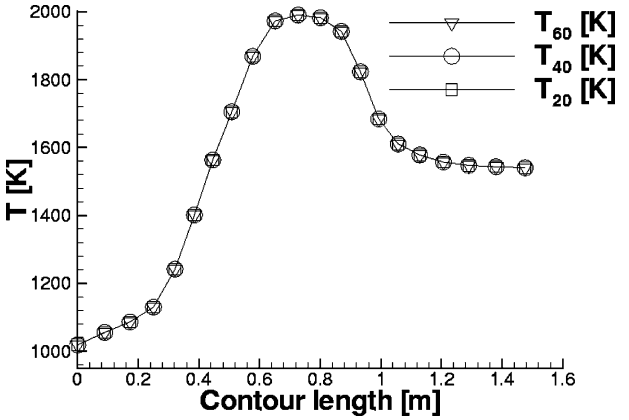

Fig. 15 Temperature distribution at the surface of COLIBRI for three different TPS grid resolutions.

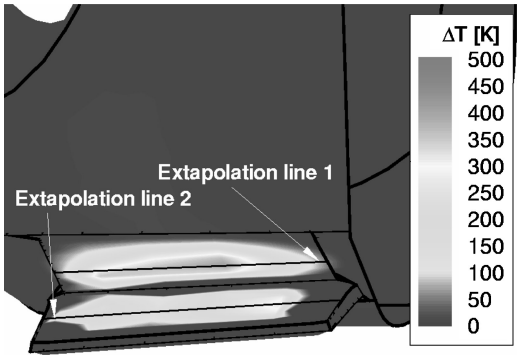

Fig. 16 Temperature difference at the cavity region of the body flap of the X-38.

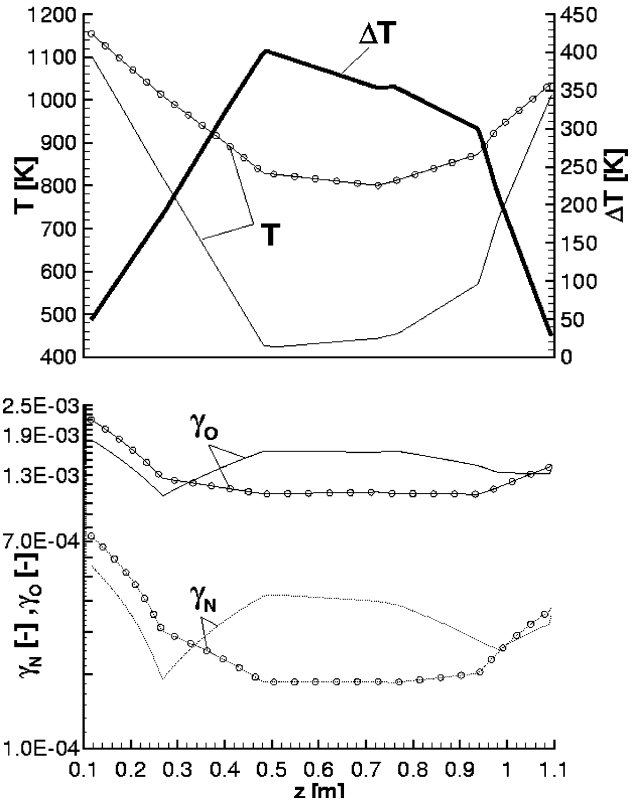

Fig. 17 Temperature, temperature difference distribution, and recombination coefficients along extrapolation line 1 with and without radiative exchange at the surface.

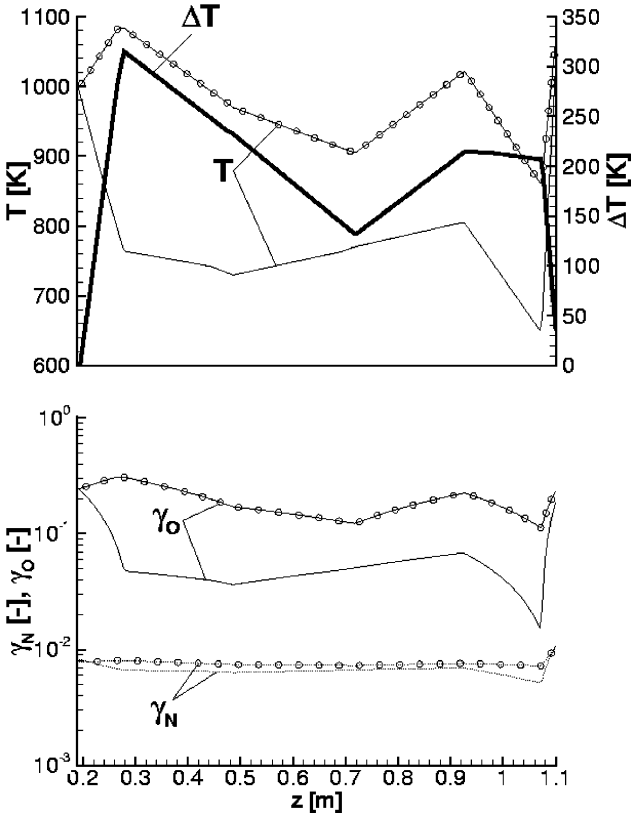

Fig. 18 Temperature, temperature difference distribution, and recombination coefficients along extrapolation line 2 with and without radiative exchange at the surface.

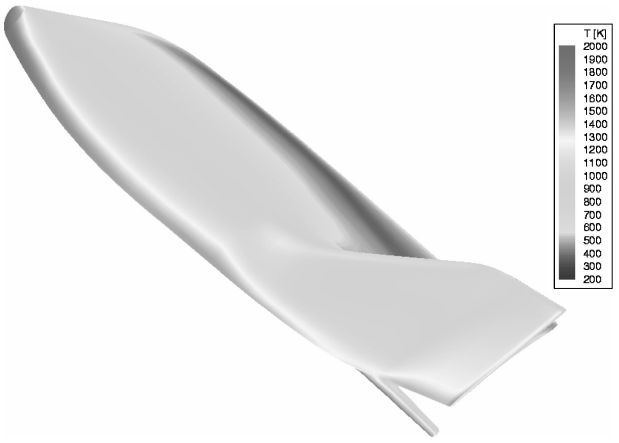

Fig. 19 Temperature distribution at the surface of the X-38 with real TPS without heat conduction within the TPS.

The results show how significant the consideration of radiative exchange and the impact it could have on the surface catalysis. Considering the pressure range in this concave zone (30–50 Pa), active oxidation of the C/SiC material is highly possible.

Heat Conduction Within the TPS of the X-38

Figures 19–21 show the temperature distribution at the surface of the X-38 with radiative exchange at the surface before and after taking the heat conduction within the TPS into account. At the first sight there are no great differences to observe; the temperature distribution has the same topology: the highest temperature is at the stagnation point region; temperature jumps caused by material change at the conjunction zones of the nose cap; pressure-driven temperature distribution at the winglet; and temperature augmentation at the angular regions of the X-38 as a result of thinner local

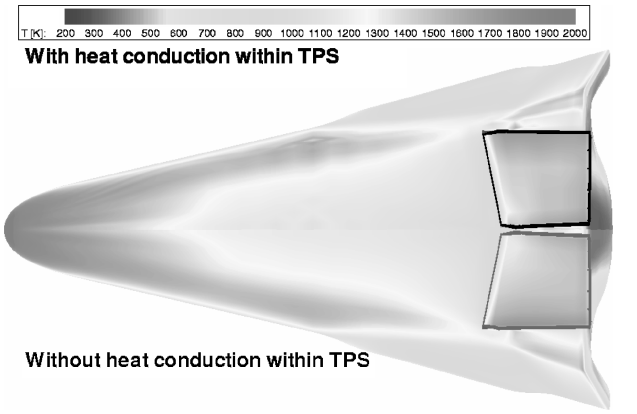

Fig. 20 Temperature distribution at the surface of windward side of the X-38 with real TPS.

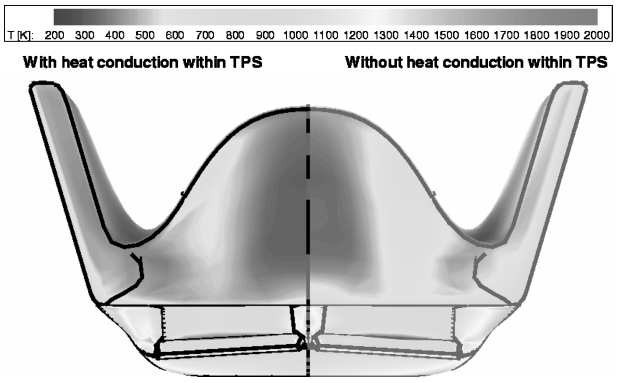

Fig. 21 Temperature distribution at the surface of the X-38 with real TPS.

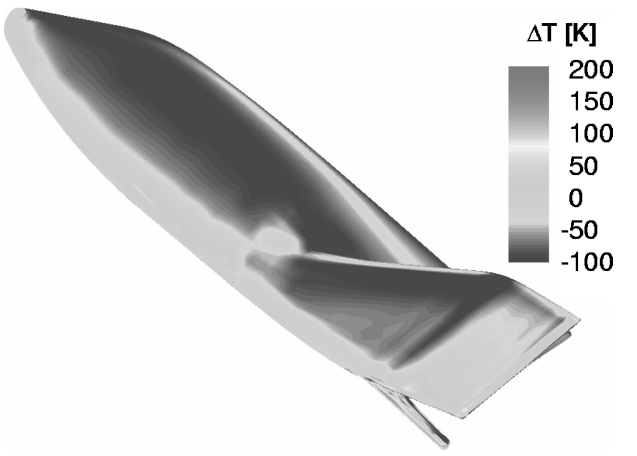

Fig. 22 Temperature differences at the surface of the X-38 before and after considering heat conduction within the TPS.

boundary layers. As we have seen for COLIBRI, the temperature is marching from high-temperature to lower-temperature regions. The temperature displacements show a three-dimensional behavior. Figure 21 gives the best view for this behavior.

Changes in surface-temperature distribution after considering the heat conduction within the TPS become obvious when taking a look at the differences between the surface temperatures of the two simulation cases. Figure 22 shows quantitatively the differences for the X-38 vehicle.

As we can see in Fig. 22, the changes are very significant, varying between -100 K and $+200$ K. There is augmentation of the temperature at the angular regions of the vehicle. The peculiarity is

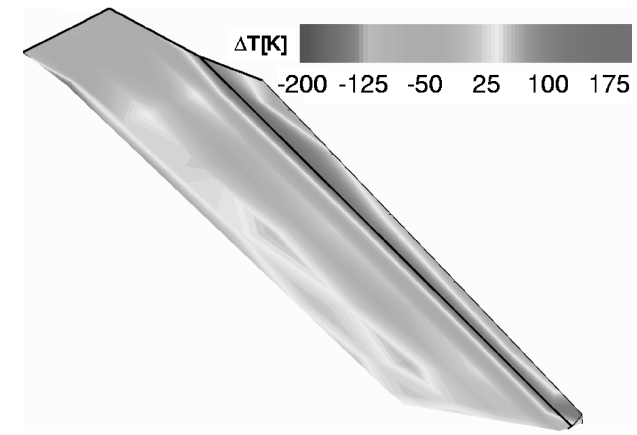

Fig. 23 Temperature differences at the windward side of the X-38 body flap before and after considering heat conduction within the TPS.

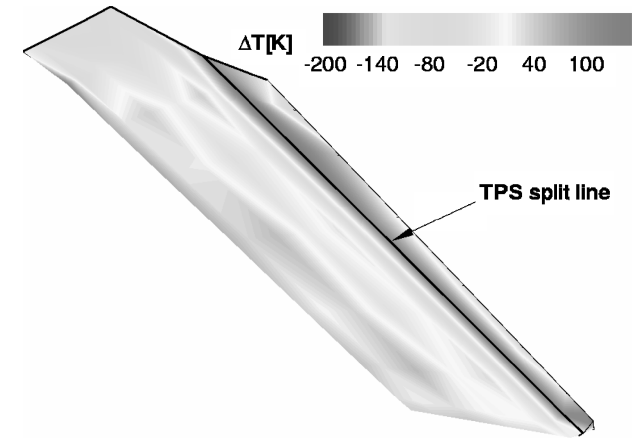

Fig. 24 Temperature differences at the windward side of the X-38 body flap before and after considering heat conduction within the TPS taking TPS split line into account.

that there are no great differences between the maximum values of the temperature distributions of the cases, but rather a displacement of the regions where they occur. In combination with catalytic reaction, as we have seen for the radiative exchange at the surface, heat conduction within TPS accelerates catalytic reactions at the surface in a significant way, so that new heat loads at the surface arise. This can be observed at the winglet. The temperature distribution at the winglet is mainly governed by pressure distribution. Adding the effect of heat conduction, the nonequilibrium gas particles, which are transported in the boundary layer and marching streamwise, recombine at surfaces further downstream. These surfaces are additionally heated by the conduction, which causes an increase in the recombination at the surface and thus an increase in the heat distribution.

Another example for the interaction between heat conduction and angular geometry is given at the body-flap edges. Here, temperature increases up to $+175$ K are observed; see Fig. 23. In case of TPS material split line at the hot edge, that is, considering the TPS material tiles insolated from each other, see Fig. 24, temperature increases up to $+120$ K can be observed. The analysis supported by Fig. 25 shows that the heat conduction accelerates the recombination of nitrogen, which dominates the temperature distribution and causes the significant temperature change at the windward side of the X-38's body flap.

As another example for the influence of the catalytic reactions at the surface in combination with heat-conduction within TPS, we consider the nose cap region, which baseline temperature is given in Fig. 26. Figures 27 and 28 show a closer view of at the temperature differences and the locations.

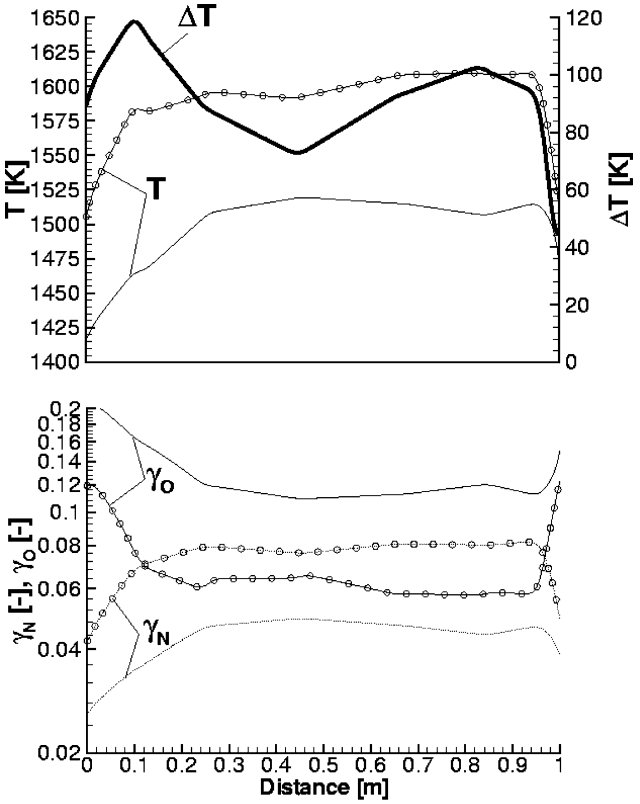

Fig. 25 Temperature, temperature difference distribution, and recombination coefficients along the split line.

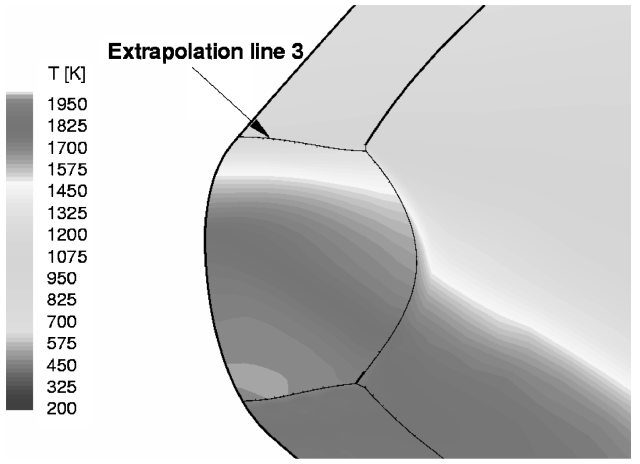

Fig. 26 Temperature distribution at the nose-cap region with heat conduction within the TPS.

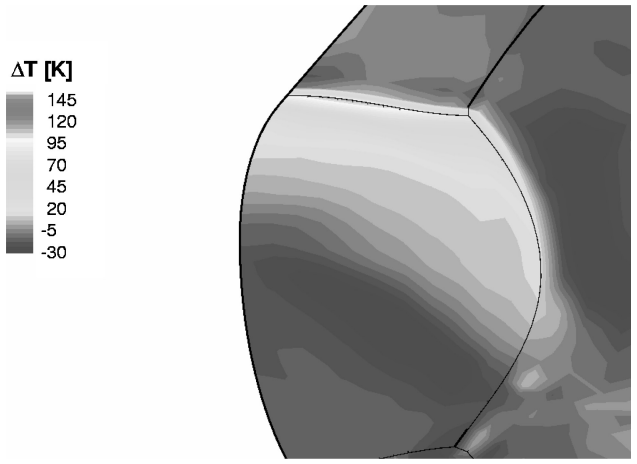

Fig. 27 Temperature difference at the nose-cap region with and without heat conduction within the TPS.

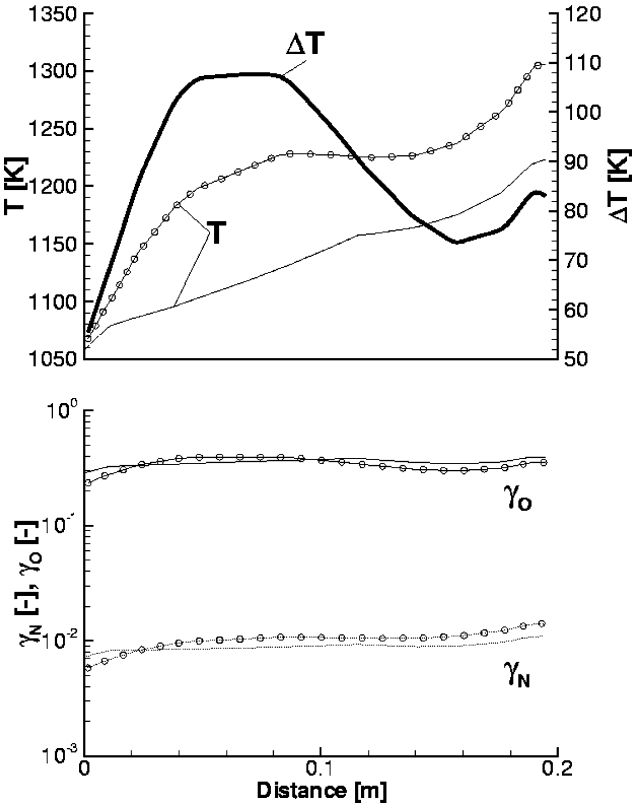

Fig. 28 Temperature, temperature difference distribution and recombination coefficients along extrapolation line 3.

We observe a temperature increase of +130 K. The catalytic behavior of TPS material experiences changes, especially the recombination of the atomic nitrogen. As we have seen for the extrapolation line 1, the catalysis is not responsible for the temperature augmentation. So the increase is purely contributed to simple heat conduction.

The gas state is also influenced by the heat conduction within the TPS. As final results, we would like to show the changes in composition and temperature in the gas along stagnation streamline. The solid lines of Figs. 29 and 30 denote the variables of the case where the heat conduction within the TPS has been taken into account. For the stagnation streamline the maximum difference in translational temperature is +250 K, where the molecular oxygen concentration is also higher. As expected, the influence of the heat conduction only influences the gas state within the range of the boundary layer. The contribution of the Figs. 29 and 30 serves as proof of the coupling with the gas phase. This should be important for the absorption's behavior of the species if gas radiation is accounted for the simulations.

Accuracy of the Results

Previous results with the URANUS code showed a good agreement with the simulated and the in-flight measured heat load distributions.[2] However, the accuracy was within the range of 5% on the windward side heat distribution. The developed modeling in this paper considering the radiative heat exchange at the surface and the heat conduction within the TPS material delivers the expected results. However, for more accurate predicting of the heat loads using the models discussed here, some issues have to be considered.

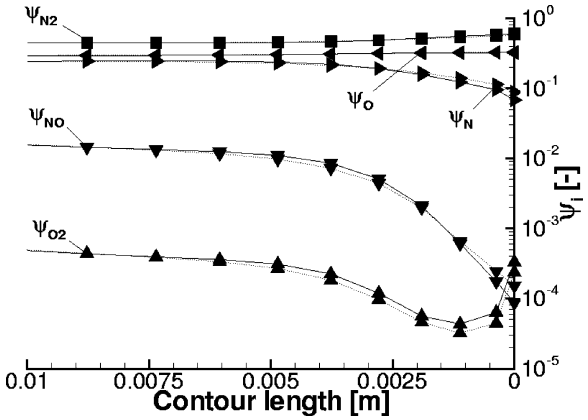

Fig. 29 Molar fraction of the species along stagnation streamline: · · · ·, with TPS heat conduction.

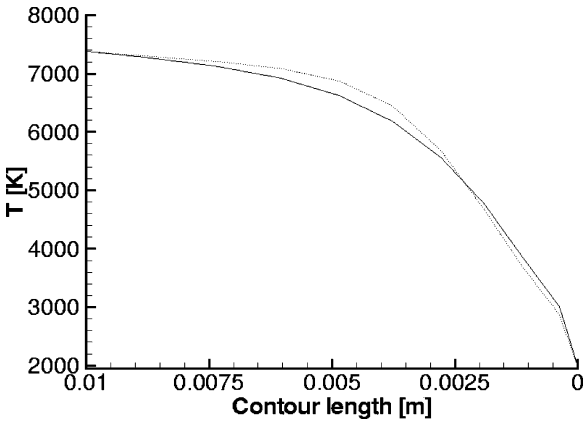

Fig. 30 Translational temperature along stagnation streamline: · · · ·, with TPS heat conduction.

First, the heat-conduction effects do not consider the real design property of the TPS tiles and the way they are connected on the space vehicle. The simulations consider large parts of the same material coating to be accumulated on one place of tile without chinks in between. Even though the modeling can consider any kind of isolation or chink, the feasibility of such an approach is not practical because the mesh should give the exact surface contour of an entire space vehicle with a detail level, which cannot be computed.

Second, the recombination coefficients used in the simulations are not pressure dependent. So, for the cavity region, where the pressure sinks dramatically, the recombination coefficients also have to be pressure dependent. Nevertheless, temperature increases obtained in this article in the cavity region still have, at least, their quantitative legitimacy.

Summary

Models that describe radiative exchange at the surface and thermal heat conduction within TPS material have been successfully derived and implemented in the P-MB URANUS code, supplementing the catalysis modeling at the surface. The models have been demonstrated in the case of the X-38 reentry vehicle. The models showed significant temperature changes at the surface in combination with the strong interaction with the catalysis of the TPS material. The heat conduction showed a temperature increase of up changes +175 K at the surface of the X-38 with a real TPS coating depending on the insulation assumption. Such influence cannot be neglected. The radiation model showed a dramatic increase of +420 K, in combination with heat conduction within the TPS +500 K at the body-flap cavity region of X-38.

The modeling also influences the gas state within the range of the boundary layer in significant way. The models do not take heat generation in the TPS into account. After implementing the newly developed catalysis model, which allows many more reactions at the surface and predicts heat-generation terms at the surface, we are aiming to include these terms in the TPS heat-conduction model. In addition, a more reliable prediction of the surface-temperature distribution can be obtained. Furthermore, simulations with reentry vehicles with much more interesting nonconvex geometry such as EXPERT are in preparation.

Acknowledgments

The authors thank Deutsche Forschungsgemeinschaft DFG and ESA for their support. Also the funding through the TETRA-program is acknowledged. M. Fertig is acknowledged for his advice during the development of the models presented here. The authors also thank G. Herdrich and T. Laux for experimental data they provided.

References

[1]Stewart, D., "Determination of Surface Catalytic Efficiency for Thermal Protection Materials—Room Temperature to Their Upper Use Limit," AIAA Paper 96-1863, June 1996.

[2]Fertig, M., and Frühauf, H.-H., "Detailed Computation of the Aerothermodynamic Loads of the MIRKA Capsule," *Proceedings of the 3rd European Symposium on Aerothermodynamics for Space Vehicles*, ESTEC, Noordwijk, The Netherlands, 1998, pp. 703–710.

[3]Frühauf, H.-H., Infed, F., Fertig, M., and Olawsky, F., "Thermal Loads for the Experimental Vehicle X-38," *Proceedings of the 4th European Symposium on Aerothermodynamics for Space Applications*, 2002, pp. 529–535.

[4]Infed, F., and Auweter-Kurtz, M., "Simulation of Hypersonic Flows in Thermo Chemical Nonequilibrium Around Re-Entry Vehicle X-38 with the URANUS Code," *Journal of Space Technology*, Vol. 24, No. 2, 2004, pp. 81–93.

[5]Burkhardt, J., Gräßlin, M., and Schöttle, U., "Impact of Mission Constraints on Optimal Flight Trajectory for the Lifting Body X-38," AIAA-Paper 99-4167, Aug. 1999.

[6]Gräßlin, M., Schöttle, U., Wallner, E., Well, K., and Burckhardt, J., "Adaptive Guidance and Control Algorithms applied to the X-38 Reentry Mission," International Astronautical Congress, Paper IAC-02-A.1.08, Oct. 2002.

[7]Auweter-Kurtz, M., "Test Plan and Test Report (TSP/TR) for PYREX-Kat38/FM," Inst. of Space Systems, Univ. of Stuttgart, X38-IRS-TSP/TR-PY011, Stuttgart, Germany, March 2000.

[8]Fertig, M., and Frühauf, H.-H., "Strömungs-Struktur-Wechselwirkung bei der X-38 Klappe (TETRA AP 21365)," Inst. of Space Systems, Univ. of Stuttgart, IRS-02 P 08, Stuttgart, Germany, Dec. 2002 (in German).

[9]Frühauf, H.-H., Fertig, M., Olawsky, F., and Bönisch, T., "Upwind Relaxation Algorithm for Reentry Nonequilibrium Flows," *High Performance Computing in Science and Engineering 99*, Springer-Verlag, Berlin, 2000, pp. 365–378.

[10]Chou, S. Y., and Baganoff, D., "Kinetic Flux-Vector Splitting for the Navier-Stokes Equations," *Journal of Computational Physics*, Vol. 130, No. 2, 1997, pp. 217–230.

[11]Knab, O., Frühauf, H.-H., and Messerschmid, E., "Theory and Validation of the Physically Consistent Coupled Vibration-Chemistry-Vibration Model," *Journal of Thermophysics and Heat Transfer*, Vol. 9, No. 2, 1995, pp. 219–226.

[12]Kanne, S., Knab, O., Frühauf, H.-H., and Messeschmid, E. W., "The Influence of Rotational Excitation on Vibration-Chemistry-Vibration-Coupling," AIAA Paper 96-1802, June 1996.

[13]Fertig, M., Dohr, A., and Frühauf, H.-H., "Transport Coefficients for High-Temperature Nonequilibrium Air Flows," *Journal of Thermophysics and Heat Transfer*, Vol. 15, No. 2, 2001, pp. 148–156.

[14]Olawsky, F., Infed, F., and Auweter-Kurtz, M., "Preconditioned Newton-Method for Computing Supersonic and Hypersonic Nonequilibrium Flows," AIAA Paper 2003-3702, June 2003; also *Journal of Spacecraft and Rockets* (to be published).

[15]Frühauf, H.-H., Fertig, M., Infed, F., Kanne, S., Olawsky, F., Resch, M., and Bönisch, T., "Numerische Wiedereintritts-Aerothermodynamik, Arbeits- und Ergebnisbericht, Sonderforschungsbereich 259 Hochtemperaturprobleme Rückkehrfähiger Raumtransportsysteme," C3. Stuttgart, 2001, pp. 355–389 (in German).

[16]Walshaw, C., Cross, M., and Everett, M., "Parallel Dynamic Graph Partitioning for Adaptive Unstructured Meshes," *Journal of Parallel Distributed Computing*, Vol. 47, No. 2, 1997, pp. 102–108.

[17]Daiß, A., Frühauf, H.-H., and Messerschmid, E.W., "Modeling of Catalytic Reactions on Silica Surfaces with Consideration of Slip Effects," *Journal of Thermophysics and Heat Transfer*, Vol. 11, No. 3, 1997, pp. 346–352.

[18]Infed, F., Olawsky, F., and Auweter-Kurtz, M., "Stationary Coupling of 3D Hypersonic Nonequilibrium Flows and TPS Structure with URANUS," AIAA Paper 2003-3984, June 2003.

[19]Zienkiewicz, O. C., *The Finite Element Method*, McGraw–Hill, New York, 1977, pp. 386–392.

[20]Patanka, Suhas V., *Numerical Heat Transfer and Fluid Flow*, Taylor and Francis, Philadelphia, 1980, p. 58.

[21]Shewshuk, J. R., and Ghattas, O., "A Compiler for Parallel Finite Element Methods with Domain-Decomposed Unstructured Meshes," *Proceedings of the Seventh International Conference on Domain Decomposition Methods in Scientific and Engineering Computing 1994*, edited by D. E. Keyes and J. Xu, Vol. 180, Contemporary Mathematics, American Mathematical Society, Providence, RI, 1994, pp. 445–450.

[22]Stewart, D., "Surface Catalysis and Characterization of Proposed Candidate TPS for Access-to-Space Vehicles," NASA TM-112206, July 1997.

[23]GridPro v4.0, Program Development Corp., White Plains, NY, URL: http://www.gridpro.com [cited 5 Jan. 2004].

B. Hassan
Associate Editor